



CO Mapping of Cygnus-X—Volume Density Distribution

Jonah C. Baade , Shuo Kong , John H. Bieging , and Thomas Folkers

Steward Observatory, The University of Arizona, Tucson, AZ 85721, USA

Received 2023 August 25; revised 2023 October 25; accepted 2023 November 6; published 2023 December 20

Abstract

We present CO(2-1) and $^{13}\text{CO}(2-1)$ maps of the Cygnus-X molecular cloud complex using the 10 m Heinrich Hertz Submillimeter Telescope. The maps cover the southern portion of the complex, which is strongly impacted by the feedback from the Cygnus OB2 association. Combining CO(1-0) and $^{13}\text{CO}(1-0)$ maps from the Nobeyama 45 m Cygnus-X CO Survey, we carry out a multitransition molecular line analysis with RADEX and derive the volume density of velocity-coherent gas components. We select those components with a column density in the power-law tail part of the column density probability distribution function (N-PDF) and assemble their volume density into a volume density PDF (ρ -PDF). The ρ -PDF exhibits a power-law shape in the range of $10^{4.5} \text{ cm}^{-3} \lesssim n_{\text{H}_2} \lesssim 10^{5.5} \text{ cm}^{-3}$ with a fitted slope of $\alpha = -1.12 \pm 0.05$. The slope is shallower than what is predicted by simulations of rotationally supported structures or those undergoing gravitational collapse. Applying the same analysis to synthetic observations with feedback may help identify the cause of the shallow slope. The ρ -PDF provides another useful benchmark for testing models of molecular cloud formation and evolution.

Unified Astronomy Thesaurus concepts: [Interstellar medium \(847\)](#); [Giant molecular clouds \(653\)](#); [Radiative transfer \(1335\)](#); [Radiative transfer equation \(1336\)](#); [Radiative transfer simulations \(1967\)](#); [Molecular clouds \(1072\)](#); [Photodissociation regions \(1223\)](#); [Stellar feedback \(1602\)](#)

1. Introduction

The density structure of a giant molecular cloud (GMC) is crucial to our understanding of the star formation in the cloud. Because of shocks from supersonic turbulence, a GMC typically contains local overdense regions that are prone to gravitational collapse. The collapsing loci will see the birth of the next-generation young stars. Therefore, a census of these clouds' densities, in particular for those exceeding the critical value for collapse, is extremely useful for estimating star formation properties, including, e.g., the star formation efficiency.

The density probability distribution function (hereafter ρ -PDF) is particularly helpful for the census. Due to the multiplicative nature of the density fluctuation, the ρ -PDF of a GMC with supersonic turbulence is well approximated by a log-normal distribution (Vazquez-Semadeni 1994; Padoan et al. 1997) for relatively lower densities. The approximation remains valid when considering chemistry (Glover et al. 2010; Federrath 2013) and magnetic fields (Lemaster & Stone 2008; Padoan & Nordlund 2011).

For higher densities that are gravitationally unstable, the ρ -PDF is skewed to a power-law shape. Using numerical and analytical methods, Kritsuk et al. (2011, hereafter K11) showed that the power-law relation originates from the power-law density profile of spherically symmetric collapsing regions (also see Girichidis et al. 2014; Jaupart & Chabrier 2020). For a spherically symmetric density profile $\rho \propto r^{-n}$, the ρ -PDF has the form of $P(\rho) \propto \rho^{-3/n}$, i.e., a steeper collapsing density profile gives rise to a shallower power-law ρ -PDF. For instance, a collapsing isothermal sphere with a profile of $\rho \propto r^{-2}$ (e.g., Shu 1977) would show a power-law ρ -PDF of $P(\rho) \propto \rho^{-1.5}$. For a collapsing turbulent core with $\rho \sim r^{-1.5}$ (Murray & Chang 2015), the ρ -PDF is $P(\rho) \propto \rho^{-2}$. K11 also

observed a density profile of $\rho \propto r^{-3}$ for rotationally supported cores at higher densities ($n_{\text{H}_2} > 5 \times 10^9 \text{ cm}^{-3}$), which indicated a ρ -PDF of $P(\rho) \propto \rho^{-1}$. The PDF at the end of the simulation in K11 showed two power laws, one being $P(\rho) \propto \rho^{-1.67}$ at intermediate densities, the other $P(\rho) \propto \rho^{-1}$ at higher densities. These results were confirmed by the recent simulation work from Khullar et al. (2021). Including magnetic fields, Collins et al. (2011) found a ρ -PDF power-law slope of -1.64 , which is consistent with the power law at intermediate densities in K11.

Observationally, the density structure is usually measured by the column density (N-PDF), which is directly observable along each line of sight through, e.g., dust emission/absorption and molecular line emission (e.g., Kainulainen et al. 2009; Froebrich & Rowles 2010; Schneider et al. 2013; Murase et al. 2023). N-PDFs typically exhibit a log-normal profile at relatively low extinctions with or without a power-law tail at higher extinctions. The log-normal profile is believed to be a result of supersonic turbulence (e.g., Vazquez-Semadeni 1994; Federrath et al. 2008; Ballesteros-Paredes et al. 2011), while the power-law tail can result from pressure confinement (e.g., Passot & Vázquez-Semadeni 1998) and/or gravitational collapse (e.g., Cho & Kim 2011; Ward et al. 2014).

Recently, Schneider et al. (2022, hereafter S22) measured N-PDF in 29 Galactic regions using Herschel dust emission maps. They found that the clouds in general were well fit with a sum of two log-normal profiles at lower densities and a sum of two power-law tails at higher densities. The massive clouds tend to have a shallower second power law, consistent with the findings in K11 simulations and Schneider et al. (2015) observations. The shallower power law is probably due to physical mechanisms that hinder gas concentration, including, e.g., rotation, magnetic fields, and (massive) stellar feedback.

In this paper, we aim to construct the ρ -PDF, instead of the N-PDF, of the massive star-forming cloud Cygnus-X. While N-PDF is more straightforward to measure in observations, ρ -PDF is more directly linked to the underlying physics of the

density structure. The ρ -PDF also provides a pathway to estimating the star formation efficiency, especially in active star-forming clouds that are dominated by gravity (Kainulainen et al. 2014).

To measure the ρ -PDF, we simply estimate the gas density (n_{H_2}) that is responsible for the molecular line emission through detailed radiative transfer modeling. As will be introduced in Section 3, we use multitransition CO and ^{13}CO lines for the modeling. The assumption is that the molecular line emission is solely excited through the collisional interaction with the partner H_2 . The advantage of the method is that the derived H_2 volume density n_{H_2} does not suffer the depletion problem that happens to molecular column-density measurements (e.g., Goodman et al. 2009), as the freeze-out of H_2 ice on dust grains is rather limited (Wakelam et al. 2017), if there is any (see discussions in Seligman & Laughlin 2020). The use of molecular lines also alleviates the problem of projection effects in N-PDF studies (e.g., Schneider et al. 2016; Wang et al. 2020; Murase et al. 2023).

The Cygnus-X molecular cloud complex, at a distance of ~ 1.4 kpc (Rygl et al. 2012), is an active star-forming region with ample dense gas (total mass $\sim 10^6 M_{\odot}$, Schneider et al. 2006) and strong feedback from clusters of O/B stars (Reipurth & Schneider 2008; Wright et al. 2015). It provides an unprecedented cosmic lab for the study of cloud density distribution in the presence of the interaction between gravity and massive stellar feedback. As introduced earlier, a ρ -PDF typically contains a power-law profile at relatively higher densities, which is caused by gravitational collapse. However, we lack quantitative knowledge about how feedback shapes the ρ -PDF. Qualitatively, for instance, an expanding H_{II} region sweeps the vicinity of the driving massive star and creates compressed, high-density gas, potentially flattening the power law. Schneider et al. (2015) and Stutz & Kainulainen (2015) observed shallower power-law PDF in clouds with stellar feedback. In this paper, with the measurement of the ρ -PDF in Cygnus-X, we aim to examine how the strong feedback from the O-stars (re)shapes the density distribution. We will focus on the power-law part of the ρ -PDF at relatively high densities.

In the following, we first describe our data collection in Section 2, including our newly acquired maps of CO(2-1) and ^{13}CO (2-1) using the Heinrich Hertz Submillimeter Telescope (SMT) and the publicly available Nobeyama 45 m Radio Observatory (hereafter NRO45) maps of CO(1-0) and ^{13}CO (1-0). Then, in Section 3, we describe in detail our multiline fitting methods for deriving the gas volume density. Next, we report our findings in Section 4. Finally, we discuss and conclude in Sections 5 and 6, respectively.

2. Observations and Data Reduction

2.1. SMT

The CO(2-1) and ^{13}CO (2-1) lines were observed with the Heinrich Hertz Submillimeter Telescope (SMT¹) on Mt. Graham, Arizona, at an elevation of 3200 m. The facility is operated by the Arizona Radio Observatories (ARO), a division of Steward Observatory at the University of Arizona. The basic flow of observation and data reduction follows that described in Bieging et al. (2010, 2014, 2016). In the following, we comment on several key aspects.

We map the southern part of the Cygnus-X complex from November 2019 to June 2021 with a beam size of $32''$. Figure 1 shows the mapped region in the green polygon. The region is divided into multiple $10' \times 10'$ rectangles, each being mapped in an on-the-fly (OTF) session for about 1.5 hr. We use the dual-polarization ALMA Band 6 prototype receiver with the spectrometer that simultaneously observes CO(2-1) in the upper sideband and ^{13}CO (2-1) in the lower sideband. The data were calibrated and processed as described in Bieging et al. (2014). Telescope pointing was checked and corrected as necessary approximately every few hours. We use the quarter-MHz filter bank for ^{13}CO (2-1), which gives a spectral resolution of 0.34 km s^{-1} . Because of the broad line width of the CO(2-1) line, we use the MHz filter bank for the line, to get the baseline fitting. Typical rms noise values per pixel were 0.09 K in main-beam brightness temperature per 1.3 km s^{-1} for CO(2-1) and 0.10 K per 0.34 km s^{-1} for ^{13}CO (2-1).

2.2. Nobeyama 45 m Data

In this paper, we make use of the Nobeyama 45 m Cygnus-X survey data from Yamagishi et al. (2018) and Takekoshi et al. (2019). This survey utilized the four-beam receiver FOREST on the NRO45 telescope to carry out a multiline mapping of the Cygnus-X North and South regions (see the white polygon in Figure 1). The survey data is publicly available here.² For our study, we acquired the cubes for the CO(1-0) and ^{13}CO (1-0) transitions. Out of the several data products, we selected cubes with a beam size of $23''$, a spectral resolution of 0.25 km s^{-1} , and a velocity range of -40 to 40 km s^{-1} . The choice gives the best match with our SMT data and covers the velocity range of Cygnus-X (Schneider et al. 2006). The median rms noises for the CO(1-0) and ^{13}CO (1-0) data are 2.37 K and 0.95 K, respectively. Using Gaussian kernel methods from the `spectral-cube` and `FITS_tools` Python packages, we smoothed the NRO45 cubes to an effective angular resolution of $32''$ and a spectral resolution of 0.34 km s^{-1} , to match the SMT ^{13}CO (2-1) map. We then reprojected them to the same spatial and spectral coordinates as the SMT map, with a final pixel size of $10''$ and a velocity range of -15.9 to 25.9 km s^{-1} .

3. Methods

We use the radiative transfer program RADEX³ (van der Tak et al. 2007) to model the observation and estimate the gas volume density n_{H_2} . RADEX takes four parameters relevant to our study in its input: the kinetic temperature of the gas (T_{kin}), the volume density of the collision partner (n_{H_2}), the molecular column density ($N_{^{13}\text{CO}}$), and the FWHM line width of the observed velocity component.

For this pilot study, our strategy is to focus on gas parcels that are in local thermodynamic equilibrium (LTE), so that the volume density n_{H_2} is the only unknown parameter for RADEX. Typically, LTE gas tends to be relatively dense ($n_{\text{H}_2} \gtrsim 10^4 \text{ cm}^{-3}$) with optically thick CO lines. We analyze the aligned SMT and NRO45 cubes pixel by pixel, fitting ^{13}CO lines for each. We can approximate the gas kinetic temperature with the CO line excitation temperature. Then, the ^{13}CO column density can be estimated with an LTE equation for the relatively optically thin ^{13}CO lines. The ^{13}CO line width can be obtained through line fitting. With this information, n_{H_2}

¹ <https://aro.as.arizona.edu/?q=facilities/submillimeter-telescope>

² <https://www.nro.nao.ac.jp/~nro45mrt/html/results/data.html>

³ <https://home.strw.leidenuniv.nl/~moldata/radex.html>

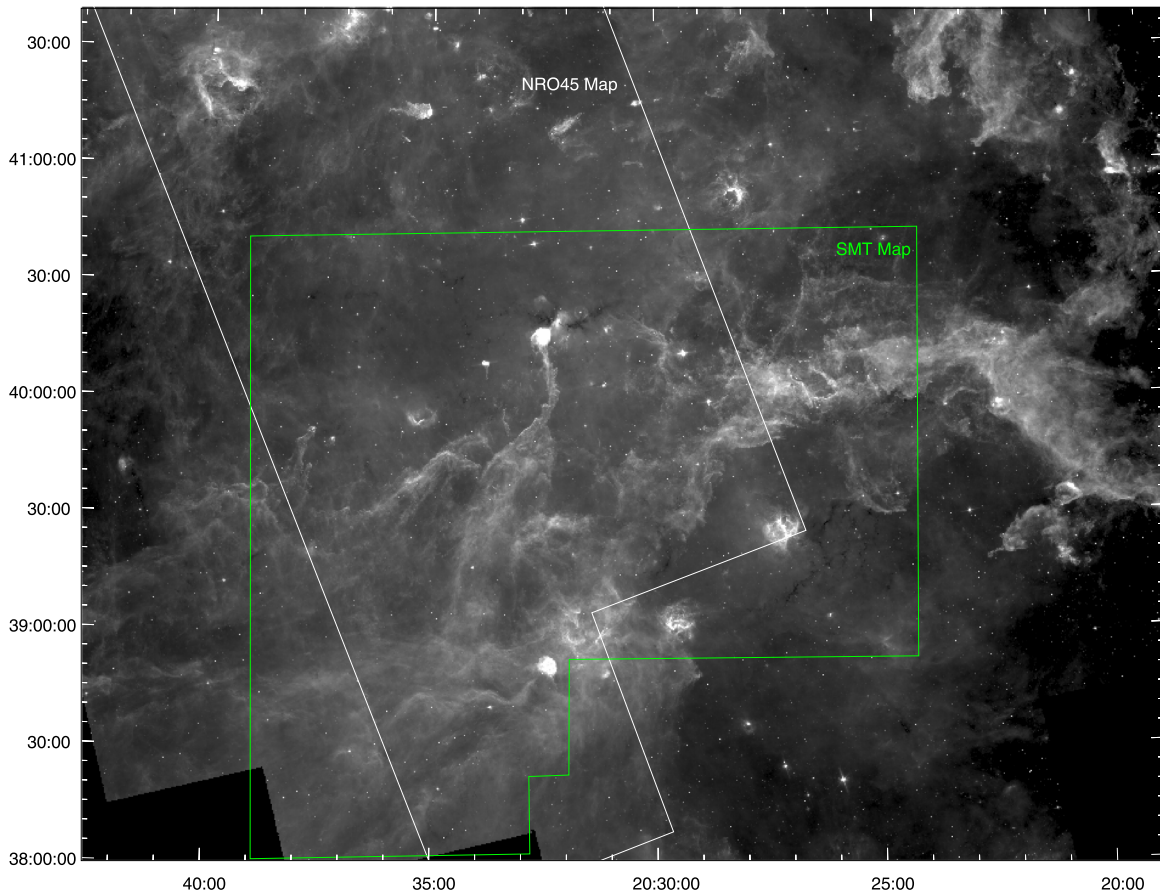


Figure 1. Spitzer $8\ \mu\text{m}$ image of Cygnus-X from the Spitzer Legacy Survey of the Cygnus-X Region (Beerer et al. 2010; Kryukova et al. 2014). The white polygon shows the NRO45 mapping area from the Nobeyama 45 m Cygnus-X CO Survey (Yamagishi et al. 2018; Takekoshi et al. 2019). The green polygon shows the SMT mapping area. Our analysis is done in the overlapping region.

becomes the only free parameter, and by varying it we can find a best-fit volume density for the observed emission. The complete procedure is as the following:

1. We use the⁴ *astrodendro* package (Rosolowsky et al. 2008) to find all velocity components in CO(1-0), CO(2-1), ^{13}CO (1-0), and ^{13}CO (2-1).
2. Using the *astrodendro* results as an initial guess, we fit all four lines with Gaussian profiles and get the peak intensity and the velocity dispersion for each velocity component.
3. We cross-match the velocity components between the four lines and keep the components that exist in all of them. Such overlaps between components that emit in all four lines are hereafter referred to as sets of components.
4. Assuming an optically thick condition, we compute the excitation temperature T_{ex} for both CO(1-0) and CO(2-1) and keep the sets whose T_{ex} agrees within 30%.
5. We compute ^{13}CO column density $N(^{13}\text{CO})$ with the CO T_{ex} , assuming LTE. We keep the sets whose $N(^{13}\text{CO})$ are greater than $7 \times 10^{15}\text{cm}^{-2}$, to make sure we are in the power-law regime based on the N-PDF in Schneider et al. (2016). We chose to focus on this power-law regime because our method is less sensitive to low-density gas.
6. With the derived T_{ex} , $N(^{13}\text{CO})$, and ^{13}CO line dispersion, we carry out RADEX modeling (van der Tak et al. 2007) of the ^{13}CO line emission with an initial guess of n_{H_2} .

7. We iterate n_{H_2} to best match the ^{13}CO (1-0) and ^{13}CO (2-1) line emission between RADEX and observations.
8. We confirm the validity of LTE by checking the T_{ex} between RADEX and observations.

Below, we expand on these steps in more details.

3.1. Fitting and Selecting Components

In each pixel, spectra in any or all of the four transitions could have multiple peaks centered at different LSR velocities, assumed to correspond to different dense regions along the line of sight. We isolated these peaks using the *astrodendro* package (Step 1), using an absolute threshold of 3σ , where σ is the pixel-based noise. Each molecular line in each pixel had its own value of σ , calculated from velocity ranges where the corresponding cubes did not have any apparent bright regions. These ranges were (21, 26) km s^{-1} for CO(1-0); (36, 100) km s^{-1} for CO(2-1); (-16, -11) and (18, 26) km s^{-1} for ^{13}CO (1-0); and (-16, -11) and (18, 26) km s^{-1} for ^{13}CO (2-1). Pixels with any lines where $\sigma > 2.5\text{ K}$, which appeared only around the edges of the data cubes, were discarded. We use a relative threshold of 1.5σ above the surroundings in velocity space, and a minimum peak width of 3 spectral pixels (2 for the CO(2-1) map, which had a factor of 4 lower spectral resolution) for *astrodendro*.

We then used the *curve_fit* method from the *scipy.optimize* package to fit a sum of Gaussian components to each spectrum (Step 2), using the peaks identified by *astrodendro* to provide initial values for the fit and determine

⁴ <http://dendrograms.org/>

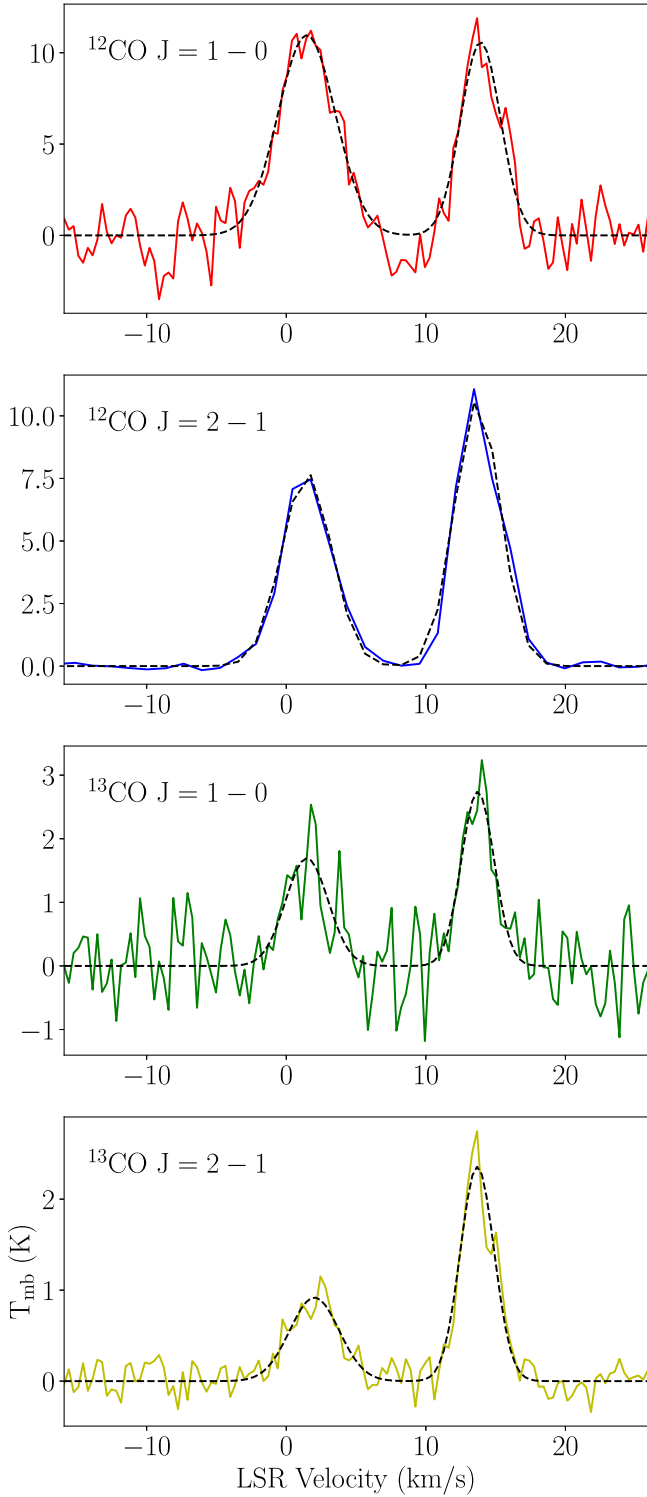


Figure 2. Plots illustrating Gaussian fit results for the pixel at (R.A., decl.) = (20^h35^m26^s, 38°27′31″). The line data are shown as colored curves, while the black dashed line shows the fitted Gaussians. Our program assigned the peaks centered at 2 and 14 km s⁻¹ into two sets.

the number of peaks to fit. Figure 2 shows an example of the fitting. If any spectrum out of the four needed more than five components to be adequately fit, we discarded that pixel, under the assumption that the data there were too noisy for a reliable analysis. The peak-fitting approach sometimes fits a low, wide component to the data rather than a small but strong component to match a peak. We excluded these components by discarding

any Gaussians that did not reach 3 σ above the pixel’s noise level, for consistency with the results from *astrodendro*.

Subsequent steps in our data analysis required peak temperatures from all four transitions, so we removed Gaussian components that appeared in only some lines but not in others at the same velocities (Step 3). To do this, we constructed a simple hierarchy in which every Gaussian component in the ¹³CO(2-1) line was matched to the closest component in ¹³CO(1-0), then to CO(2-1), and then CO(1-0). Using the standard velocity deviation σ_v of each Gaussian in sequence, we counted pairs of components as aligned if the “later” peak was within $2\sigma_v$ in velocity of the “earlier.” We also excluded all components that shared matches with each other, to avoid situations where a pair of components in one line appeared fully inside a single component in another. After all of these exclusions, we were left with only sets of nested, solitary components at similar velocities, assumed to correspond to a single dense region each. We counted 195,344 sets across 175,592 pixels before further exclusions.

3.2. Physical Conditions

3.2.1. Excitation Temperature

Each set had distinct components in CO(2-1) and CO(1-0). Using their peak temperatures, we estimated two CO excitation temperatures T_{ex} (Step 4), assuming $\tau \gg 1$, with the following equation (e.g., Equation (3)) in Kong et al. 2015):

$$T_{\text{ex}} = \frac{h\nu/k}{\ln\left(1 + \frac{h\nu/k}{T_{\text{mb,p}} + J_\nu(T_{\text{bg}})}\right)}, \quad (1)$$

where $T_{\text{mb,p}}$ is the peak main-beam temperature, T_{bg} is the cosmic microwave background temperature of 2.73 K, and $J_\nu(T_{\text{bg}}) = \frac{h\nu/k}{(e^{h\nu/kT_{\text{bg}}} - 1)}$ is the Rayleigh–Jeans equivalent temperature of a blackbody of temperature T_{bg} . To limit our modeling to sets that were assumed close to thermal equilibrium and thus amenable to an LTE approximation, we included only sets for which the T_{ex} ratio of CO(2-1) and CO(1-0) was in the range 0.7-1.3. We counted 173,188 sets after this restriction.

3.2.2. ¹³CO Column Density

We used the ¹³CO(2-1) line to compute the ¹³CO column density (Step 5), assuming the LTE condition. The $J = 2-1$ transition has the advantage of not being sensitive to the excitation temperature between 10 and 40 K (see discussions in Ginsburg et al. 2011; Bieging et al. 2016). We used an LTE equation to estimate $N_{^{13}\text{CO}}$ for each set (e.g., Equations 4 and 5 in Kong et al. 2015):

$$\tau = -\ln\left(1 - \frac{\frac{T_{\text{mb}}}{h\nu/k}}{\frac{1}{e^{kT_{\text{ex}}}} - 1} - \frac{1}{e^{kT_{\text{bg}}}}}\right) \quad (2)$$

$$N = \frac{8\pi k\nu^2}{hc^3 A_{2\rightarrow 1}} \frac{e^{\frac{h\nu}{kT_{\text{bg}}}} - 1}{e^{\frac{h\nu}{kT_{\text{ex}}}} - e^{\frac{h\nu}{kT_{\text{bg}}}}} \frac{Q}{(2J+1)e^{-\frac{hB_0J(J+1)}{kT_{\text{ex}}}}} \times \frac{\int \tau(v) dv}{\int [1 - e^{-\tau(v)}] dv} \int T_{\text{mb}} dv \text{ (cm}^{-2}\text{)}, \quad (3)$$

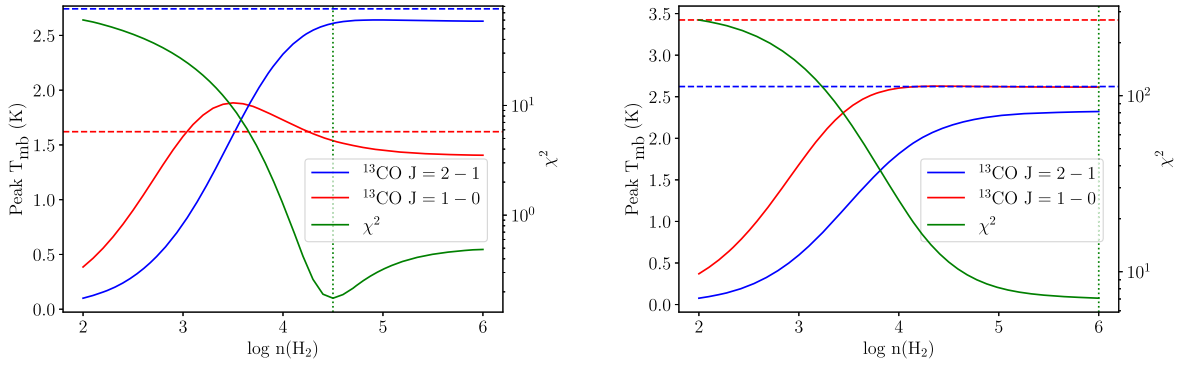


Figure 3. Plots illustrating the n_{H_2} fitting process. The left panel is for the set at the pixel at (R.A., decl.) = (20^h37^m59^s, 39°55'01''). The solid red and blue lines indicate the peak T_{mb} that RADEX outputs for each value of n_{H_2} , while the dashed lines are at the corresponding peak T_{mb} observed along the line of sight. The dotted green line, at $n = 10^{4.5} \text{ cm}^{-3}$, marks the best-fit density for this set, where the χ^2 , shown for each density in solid green and labeled on the right, is minimized. The right panel is for the set at the pixel at (R.A., decl.) = (20^h34^m37^s, 40°30'21''). The best-fit density from RADEX fitting was $n = 10^6 \text{ cm}^{-3}$, which was the highest input in our grid.

where $A_{2 \rightarrow 1}$ is the Einstein coefficient for the $J = 2-1$ transition and B_0 is the rotation constant of ^{13}CO . The excitation temperature T_{ex} used in this calculation was taken from the calculated value for the CO(2-1) transition (if it was close enough to that for the $J = 1-0$ transition in Step 4). The integrals over the main-beam temperature T_{mb} and optical depth $\tau(\nu)$ were solved using the Gaussian fits to the $^{13}\text{CO}(2-1)$ spectrum, as integrating over the spectrum itself was problematic when peaks overlapped. The partition function Q is estimated by (e.g., Equation 6 in Kong et al. 2015)

$$Q \equiv \sum_J (2J + 1) e^{-\frac{hB_0 J(J+1)}{kT_{\text{ex}}}} \simeq \frac{kT_{\text{ex}}}{hB_0} + \frac{1}{3}, \quad (4)$$

which is accurate to 10% for $T_{\text{ex}} > 5 \text{ K}$. See Mangum & Shirley (2015) for a comprehensive derivation of the column-density calculation.

We restricted our final analysis to sets with a column density $N_{^{13}\text{CO}} \geq 7 \times 10^{15} \text{ cm}^{-2}$, equivalent to $N_{\text{H}_2} \gtrsim 5 \times 10^{21} \text{ cm}^{-2}$ (assuming a H_2 -to- ^{13}CO ratio of $\sim 7 \times 10^5$; Wilson 1999). These column densities are in accordance with the regime Schneider et al. (2016) and S22 identified for a power-law tail in the N-PDF.

3.2.3. FWHM Line Width

Each set had a single Gaussian component in the $^{13}\text{CO}(2-1)$ transition. We used this component to calculate an FWHM line width (from Step 2) to enter into RADEX.

3.2.4. Kinetic Temperature

Under the assumption that the gas in the sets of interest was in LTE, we set T_{kin} for the RADEX model equal to the CO(2-1) excitation temperature (from Step 4).

3.3. RADEX Fitting

We aimed to constrain the H_2 volume density for a set by reproducing the ^{13}CO line intensities (Step 6). In RADEX, the background radiation temperature was set to 2.73 K and only H_2 was entered as a collision partner.

We configured RADEX with the default escape probabilities for a uniform sphere. As a result, we are essentially estimating the line-of-sight weighted average of the volume density of the

gas parcel that contributed to an observed set of peaks. For a parcel with a monotonic density profile, our estimation samples the volume density in a shell of the parcel. Because we are sampling the volume density at different locations across Cygnus-X, the final ρ -PDF is considered a reasonable representation of the underlying ρ -PDF of the entire cloud at the scale of the beam size (32'', corresponding to 0.22 pc at a distance of 1.4 kpc).

Because the peak radiation temperatures of $^{13}\text{CO}(1-0)$ and $^{13}\text{CO}(2-1)$ were known for each set, while n_{H_2} was unknown, we parameterized over H_2 volume density and created a grid of identical inputs with only the volume density changed. We tested a range for n_{H_2} of 10^2 – 10^6 cm^{-3} , with a logarithmic step size of 0.1 dex. We attributed a best-fit volume density (Figure 3) to a set by using the value of n_{H_2} , which produced the smallest χ^2 value between the observed and modeled peak radiation temperatures in both ^{13}CO lines (Step 7). The χ^2 is computed as

$$\chi^2 = \sum \frac{(O - E)^2}{\sigma^2}, \quad (5)$$

where O stands for observation and E stands for model. σ is the spectral noise. Currently, we are limited by having just two ^{13}CO line transitions. Adding more transitions in the future will give stronger constraints. While the vast majority ($\sim 88\%$) of sets had a local minimum χ^2 within our test range, the remainder showed χ^2 approaching an asymptote as we approached the maximum test volume density of 10^6 cm^{-3} . In the final output, these sets were placed in the 10^6 cm^{-3} group. After fitting, we counted 171,354 sets across 156,371 pixels (with the discrepancy amounting to 1834 sets that failed the integration for column density). Most of the sets were poorly fit: only 5480 of them reached $\chi^2 < 10$ at any point (including 1079 that did not have a local minimum), across 5467 pixels. However, this subset covers the main spatial extent of the region we have observed, sampling primarily from filaments and dense clouds. This provides reason to believe that the H_2 density distribution we measure reflects the true distribution throughout the denser parts of Cygnus-X South.

Our choice of cutoff at $\chi^2 < 10$ was arbitrary; it represents the best $\sim 17\%$ of fits meeting the column-density requirement, but there is no reason to suspect this is the best requirement for closeness of fit to use. We repeated the final step of the

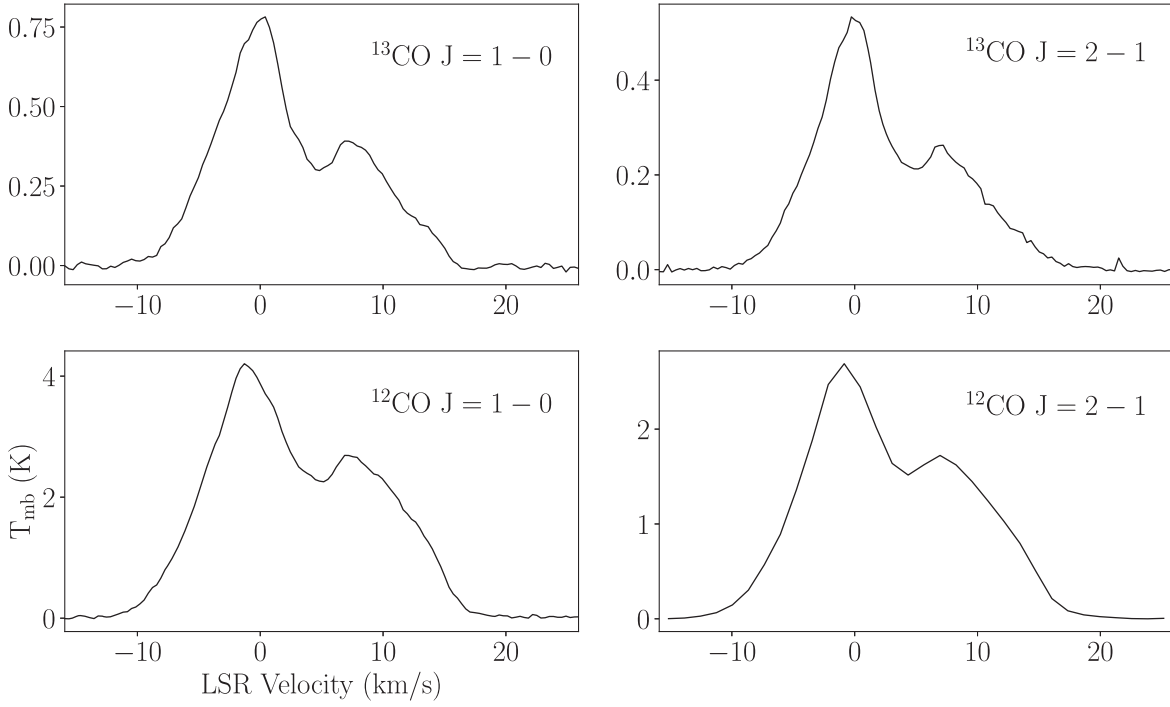


Figure 4. Averaged spectra for all four molecular lines across the entire region of mutual overlap between cubes. Pixels with $\sigma > 2.5$ K, which appeared only around the edges of the data cubes, were discarded.

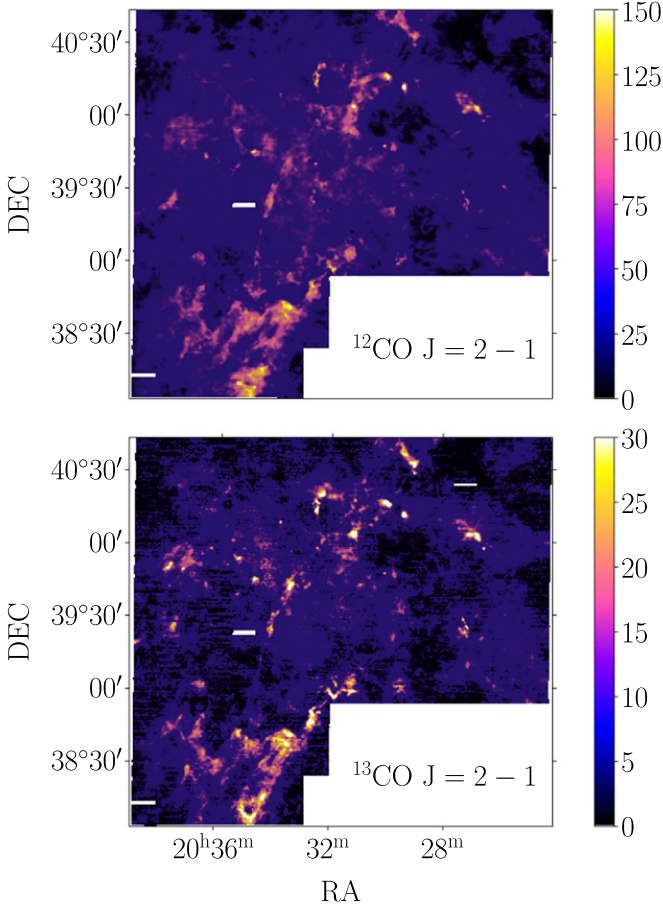


Figure 5. Integrated intensity maps for the CO(2-1) and $^{13}\text{CO}(2-1)$ data cubes. The integrated velocity range is -16 – 26 km s^{-1} . The color bar has units of K km s^{-1} .

procedure for different χ^2 cutoff values, spaced by powers of two from 2.5 to 1280. Further increasing the χ^2 cutoff value did not increase the number of sets with $N_{^{13}\text{CO}} \geq 7 \times 10^{15} \text{ cm}^{-2}$ (required by criterion 5 in Section 3). The results are shown in Figure 8 and discussed in Section 4.3.

4. Results

4.1. Global Spectra

Figure 4 shows spectra of the four lines we studied, averaged across the area where all four of these lines were present. All four lines have a strong component at or near 0 km s^{-1} and a weaker component near 7 km s^{-1} , but with significant emission across a much wider band of velocities, generally spanning the range -10 – 15 km s^{-1} . Each of the ^{13}CO lines peaks at about one-fifth the main-beam temperature of its counterpart in CO at the same transition.

4.2. Integrated Intensity and First-moment Maps

In Figure 5, we show maps of the integrated line intensity for CO(2-1) and $^{13}\text{CO}(2-1)$, both from SMT observations. In general, the integrated intensity traces the same features in both maps, and it is about five times higher in CO than in ^{13}CO everywhere.

Figure 6 shows maps of the first moment, the intensity-weighted mean velocity of the gas along the line of sight, for CO(2-1) and $^{13}\text{CO}(2-1)$. Both maps show large regions where the mean velocity is zero or slightly negative, and other regions where it is in the vicinity of 10 km s^{-1} , which is consistent with the averaged spectra in Figure 4. Some features are visible in both integrated intensity and first-moment maps: in particular, the filament at the bottom of the images is visible as a bright spot in both integrated intensity maps and as a negative-velocity region in the first-moment maps. The map in ^{13}CO is missing many pixels because the emission intensity in

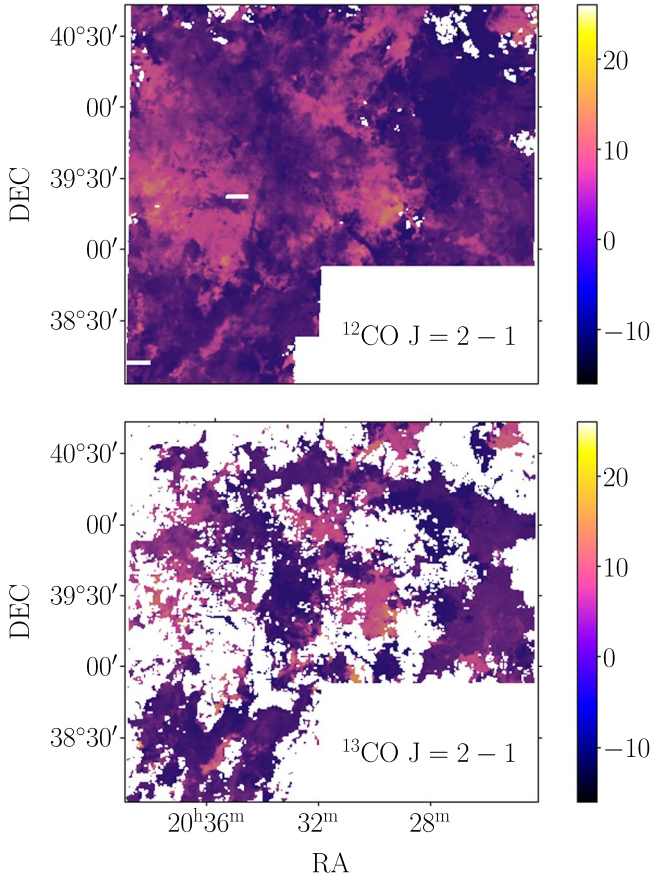


Figure 6. First-moment maps for the CO(2-1) and ^{13}CO (2-1) data cubes. The integrated velocity range is -16 – 26 km s^{-1} . Velocities in pixels with a peak intensity less than 3σ above the noise level were masked out. The color bar has units of km s^{-1} .

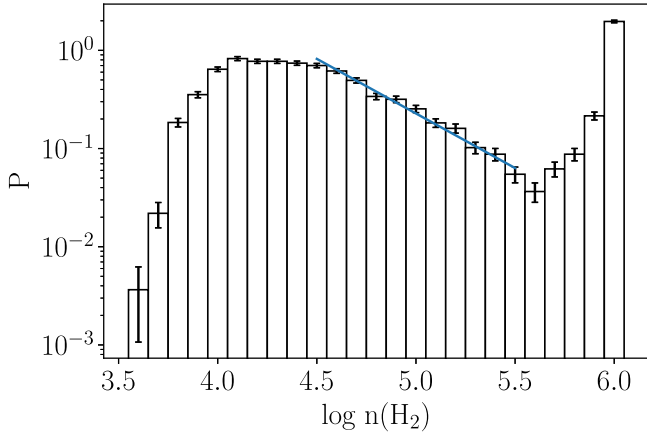


Figure 7. ρ -PDF derived from best-fit volume densities for each set. Only those with a best-fit $\chi^2 < 10$ were included. The blue line displays a linear-regression power-law fit to the data between $\log(n_{\text{H}_2}) = 4.5$ and 5.5 .

those pixels was never more than 3σ above the noise level. This is a consequence of emission in ^{13}CO being weaker overall.

4.3. ρ -PDF

In Figure 7, we show the ρ -PDF of the best-fit volume densities for the 5480 sets that reached $\chi^2 < 10$. The plot, in logarithmic scales, covers a range in $\log(n_{\text{H}_2})$ from 3.6–6.0, in

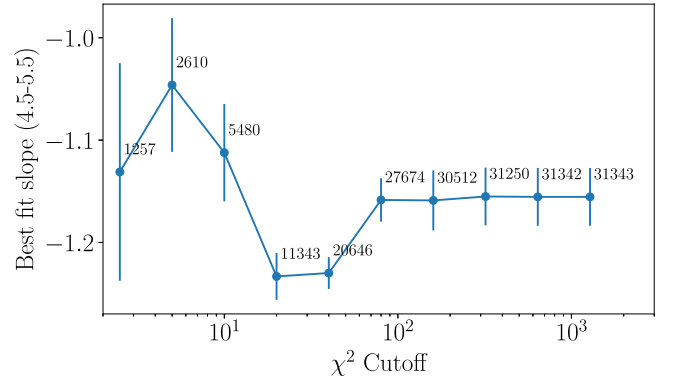


Figure 8. Slopes of the linear-regression power-law fits with varying cutoffs for the largest permitted minimum χ^2 . In all cases, the power-law fit was between $\log(n_{\text{H}_2}) = 4.5$ and 5.5 , and only sets with column density $N_{^{13}\text{CO}} \geq 7 \times 10^{15} \text{ cm}^{-2}$ were included. Numbers on the plot indicate the number of sets falling within that cutoff, with 31,343 being the total number with the required column density.

logarithmic increments of 0.1 dex; no well-fit sets had best-fit volume densities less than $10^{3.6} \text{ cm}^{-3}$. A large number of sets whose χ^2 values did not reach a local minimum within our test range, and were therefore placed in the 10^6 cm^{-3} group, can be attributed to saturation while performing the fitting with RADEX. For example, in the right panel of Figure 3, the calculated peak T_{mb} for each transition gradually approached the observed peak T_{mb} but stopped rising before they could match. This could indicate that the density is actually over 10^6 cm^{-3} in that area. For instance, Schneider et al. (2016) detected high-density tracers in the cloud. In our case, a higher transition line would break the degeneracy.

The value of the probability distribution function P at each bin was calculated from the ratio of the number of sets in it divided by the total (in this case 5480), and then divided by the bin width of 0.1 accordingly to make $\int_{3.6}^{6.0} P \text{ d log}(n_{\text{H}_2}) = 1$. We calculated a line of best fit with linear regression, using the binned volume densities as the x -coordinate in $\log(n_{\text{H}_2})$ -space and the bin heights as the y -coordinate in $\log(P)$ -space. This is consistent with the corresponding column-density log-log fit between $A_V \propto N_{\text{H}_2}$ and P for power-law tails seen in, e.g., S22.

At low densities, the distribution appears log-normal, but the shape is more likely a result of a lack of detected sets of low enough intensity to correspond to these densities. At high densities, the distribution appears to be a straight line in the log-log plot, indicating a power-law relation in the ρ -PDF ($P \propto \rho^\alpha$). A linear-regression fit between $\log(n_{\text{H}_2}) = 4.5$ and 5.5 gives a power-law slope of $\alpha = -1.122 \pm 0.048$. Above these densities, the frequency rises again until our grid's maximum volume density of $10^{6.0} \text{ cm}^{-3}$, where the greatest number of sets matched.

We produced additional plots with the same procedure but different values for the largest permitted local minimum χ^2 , from 2.5 to 1280, with the latter limit just sufficient to encompass all of the sets that met the column-density requirement $N_{^{13}\text{CO}} \geq 7 \times 10^{15} \text{ cm}^{-2}$. All of these plots showed some power-law slope between $\log(n_{\text{H}_2}) = 4.5$ and 5.5 , with a value between $\alpha = -1.0$ and -1.25 (Figure 8). Uncertainty in the slope is much greater for cutoffs below our main value of $\chi^2 = 10$ but somewhat less for cutoffs above it, with the highest cutoff, including all sets of sufficient column density, having a slope of $\alpha = -1.155 \pm 0.028$.

If there were a strong power law in the true ρ -PDF of Cygnus-X, we might expect the slope of the power-law fit to approach this value more closely for more restrictive cutoffs of χ^2 , as we would be sampling from the sets for which our modeling of volume density was most accurate. While there is no clear trend toward a specific value in Figure 8, our power-law fit slopes stay within the range between $\alpha = -1.0$ and -1.25 , which suggests that the approximate value is still relevant to our conclusions. Running our procedure on synthetic data with less natural noise could help us determine whether there is a systematic bias toward this range of slopes.

4.4. T_{ex} Consistency

To confirm the accuracy of our T_{ex} estimates for CO(2-1) and CO(1-0) for each set that we made in Section 3.2, we checked them against the T_{ex} values for $^{13}\text{CO}(2-1)$ and $^{13}\text{CO}(1-0)$ that RADEX produced alongside its calculated peak radiation temperatures for the best-fit volume density (Step 8). Under LTE conditions, all four excitation temperatures should be equal to each other and to the gas kinetic temperature in the cloud.

The results are shown in Figure 9 for all 4401 sets with minimum $\chi^2 < 10$ but that did not reach our maximum density of 10^6 cm^{-3} . (The plot excludes those that reached the highest density, because the degeneracy caused an anomalous fit; those sets tend to have error close to zero.) Almost all ($\sim 87\%$) of RADEX's ^{13}CO excitation temperatures for these sets were higher in the $J = 1-0$ line, and all were lower in the $J = 2-1$ line, than our LTE estimates. About 92% of the sets had errors below 0.3 in both lines, being consistent with our 30% T_{ex} error threshold for including them in the first place.

Because we assumed LTE when calculating T_{ex} in the first place for the CO $J = 1-0$ and $J = 2-1$ transitions, the errors between our computations for CO and RADEX's for ^{13}CO are understandable. RADEX systematically returns lower T_{ex} for the $J = 2-1$ transition than our calculations, because under the non-LTE conditions it simulated, that line is not excited as much, while it usually gives higher T_{ex} for the $J = 1-0$ line because stimulated emission at high densities contributes to T_{ex} above what LTE would predict from gas kinetic temperature alone.

5. Discussion

The shallowest ρ -PDF slope in Kritsuk et al. (2011, hereafter K11) was -1 , which was caused by rotationally supported cores⁵ at a very high density of order $n_{\text{H}_2} \sim 10^9 \text{ cm}^{-3}$. Such a density is not observed in our ρ -PDF in Figure 7 and could not be identified with these CO lines. In addition, the SMT angular resolution of $\sim 32''$ corresponds to a spatial scale of $\sim 0.22 \text{ pc}$ (assuming a distance of 1.4 kpc). Such a physical scale is not able to resolve the substructure of a dense core. Thus, the shallow slope in our measurement (-1.12 ± 0.05) is not explained by core rotation.

Stutz & Kainulainen (2015), when discussing flattened N-PDFs in the Orion A molecular cloud, suggested that feedback from O-stars in the cloud could be responsible (also see Federrath & Klessen 2013). Similarly, Russeil et al. (2013), Tremblin et al. (2014), Schneider et al. (2015), and Pokhrel et al. (2016) saw hints of shallow PDFs that were caused by

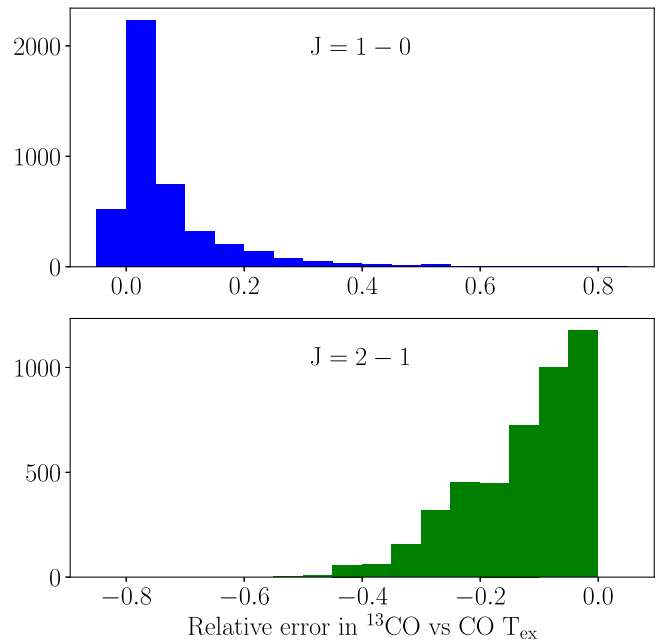


Figure 9. Histogram of relative errors between T_{ex} calculated for CO transition lines and those estimated for the corresponding ^{13}CO lines by RADEX. The horizontal scale goes up to 0.85 to include the highest outlier in the $J = 1-0$ plot (not visible).

stellar feedback. Cygnus-X is a region with its own O-star feedback, mainly from the Cygnus OB2 Association, which is to the north of the area we studied. Therefore, we tentatively attribute the shallow power law to the strong feedback environment.

Recently, S22 measured the N-PDF in Cygnus North and Cygnus South regions. Both regions were shown to have two power-law tails in the N-PDF. Cygnus North has a relatively shallow first power-law tail (slope -1.83), and its second power law is even shallower (slope -1.40), with the transition being at $A_V \sim 80 \text{ mag}$. The first N-PDF power-law tail for Cygnus South has a slope of -2.37 , which is the median value for their high-mass star-forming sample, and the second power-law tail is steeper, having a slope of -2.66 , with the transition being at $A_V \sim 37 \text{ mag}$. Our mapped region has more overlap with their Cygnus South region. Due to the limited dynamic range, our fitted ρ -PDF (Figure 7) only shows one power law. Thus, it is not clear if there is a second power law at higher densities, as shown by the N-PDF in S22. If we still follow the K11 scheme, the slope of -1.12 for the ρ -PDF should correspond to a slope of -1.19 for the N-PDF, which is shallower than the measurement from S22. While the comparison between ρ -PDF and N-PDF is not straightforward, it seems our measurement indicates a shallower PDF power-law slope than that from S22.

The apparent difference could be due to the different sampling methods (Section 3). We are distinguishing different “sets” of aligned velocity components along the same line of sight, while S22 included the total column in the Herschel map. We are only including sets in LTE (T_{ex} agrees within 30% for two ^{12}CO transitions), which intrinsically prefers denser gas. We are keeping preferentially higher column densities in order to ensure we are in the power-law regime. Considering these limits, we are effectively sampling deeply embedded denser gas that is temporarily shielded from the external radiation. But this gas probably feels the compression due to the high pressure from hot gas outside. This special sampling probably leads to

⁵ The simulations in K11 were also limited by resolutions.

the relatively shallower ρ -PDF. In the future, a comparison with synthetic observations of gas that is strongly impacted by feedback could help distinguish between such processes.

Our finding of a power-law ρ -PDF generally agrees with S22. However, Murase et al. (2023) did not find power-law profiles in ^{13}CO N-PDF in the majority of their sample. It is worth noting that they broke the Cygnus-X complex into multiple individual clouds in the position–position–velocity space. While Murase et al. (2023) considered the optical depth effect for the $J = 1-0$ transition and argued that it was a minor effect, they did not clearly show how they address the depletion effect of CO. Because they assumed LTE with median $T_{\text{ex}} \sim 10\text{--}16\text{K}$, the depletion of ^{13}CO could impact the column-density derivation and thus the N-PDF, assuming the dust temperature is similar to T_{ex} under LTE. For instance, Lewis et al. (2021) showed noticeable depletion when dust temperature was below 20 K, with the depletion factor increasing from 2 to 10 at a temperature of 12 K. If higher-column-density regions have lower temperature, the correction for depletion should be larger at high column density. Indeed, Schneider et al. (2016) found that CO depletion probably caused the N-PDF falloff at $A_V \gtrsim 40$ mag. They concluded that N-PDFs based on molecular lines were not well constrained.

6. Summary and Conclusion

We have presented OTF maps of the Cygnus-X molecular cloud complex in the $J = 2-1$ transition of both CO and ^{13}CO using the ARO SMT telescope. The maps extend from $20^{\text{h}}24^{\text{m}}$ to $20^{\text{h}}39^{\text{m}}$ in R.A. and from 38° to $40^{\circ}43'$ in decl., covering an area of ~ 10 square degrees. The mapped area overlaps with the Nobeyama 45 m Cygnus-X CO Survey in the southern portion of the complex in which we carry out a multitransition analysis for CO(1-0), ^{13}CO (1-0), CO(2-1), and ^{13}CO (2-1). Through the analysis, we have derived physical properties of the molecular gas, in particular the gas volume density.

We use `astrodendro` to identify velocity-coherent gas components (sets in each pixel) in all four lines. For each set, we fit a Gaussian profile to each line spectrum and obtain the peak intensity and line dispersion. We derive the excitation temperature T_{ex} for each CO line assuming optically thick conditions. We select sets whose T_{ex} agree within 30% between the two CO lines, such that LTE is a reasonable assumption for the sets. We then derive the ^{13}CO column density for each set. These physical properties are fed to the RADEX program, with which we iteratively find the best H_2 volume density by matching the intensities between the model and the observation for the two ^{13}CO lines. We construct the volume density probability distribution function (ρ -PDF), which shows a single power-law tail between $\log(n_{\text{H}_2}) = 4.5$ and 5.5 with a slope of $\sim -1.12 \pm 0.05$. Higher transition lines are needed to trace higher densities.

The ρ -PDF power-law slope is shallower than the theoretical values between -1.5 and -2.0 in the context of self-similar gravitational collapse (e.g., Kritsuk et al. 2011). Within the same context, the corresponding column-density PDF power-law tail is also shallower than the measurements from Schneider et al. (2022) using Herschel maps. Possible causes include the fact that Cygnus-X is strongly impacted by feedback from the OB2 association (similarly to what was found in Stutz & Kainulainen 2015) and we are specifically sampling deeply embedded dense gas. Future comparison with

synthetic observations with feedback may help clarify these causes. Our observational study of ρ -PDF provides another useful test for theories.

Acknowledgments

We acknowledge fruitful discussions with Yancy Shirley and Samantha Scibelli. The Heinrich Hertz Submillimeter Telescope is operated by the Arizona Radio Observatory, which is part of Steward Observatory at The University of Arizona. We thank Patrick Fimbres, Christian Holmstedt, Robert Moulton, Blythe Guvenen, and all the observatory staff members for helping with the data acquisition and maintaining a smooth telescope operation.

Software: Python (Oliphant 2007), SciPy (Virtanen et al. 2020), Astropy (Astropy Collaboration et al. 2013), Numpy (van der Walt et al. 2011), Matplotlib (Hunter 2007), SAOImageDS9 (Joye & Mandel 2003), RADEX (van der Tak et al. 2007), spectral-cube (Ginsburg et al. 2014).

Facilities: SMT, NRO45.

ORCID iDs

Jonah C. Baade  <https://orcid.org/0009-0009-5056-6938>
 Shuo Kong  <https://orcid.org/0000-0002-8469-2029>
 John H. Bieging  <https://orcid.org/0000-0002-6291-7805>

References

- Astropy Collaboration, Robitaille, T. P., & Tollerud, E. J. 2013, *A&A*, **558**, A33
- Ballesteros-Paredes, J., Vázquez-Semadeni, E., Gazol, A., et al. 2011, *MNRAS*, **416**, 1436
- Beerer, I. M., Koenig, X. P., Hora, J. L., et al. 2010, *ApJ*, **720**, 679
- Bieging, J. H., Patel, S., Peters, W. L., et al. 2016, *ApJS*, **226**, 13
- Bieging, J. H., Peters, W. L., & Kang, M. 2010, *ApJS*, **191**, 232
- Bieging, J. H., Revelle, M., & Peters, W. L. 2014, *ApJS*, **214**, 7
- Cho, W., & Kim, J. 2011, *MNRAS*, **410**, L8
- Collins, D. C., Padoan, P., Norman, M. L., & Xu, H. 2011, *ApJ*, **731**, 59
- Federrath, C. 2013, *MNRAS*, **436**, 1245
- Federrath, C., & Klessen, R. S. 2013, *ApJ*, **763**, 51
- Federrath, C., Klessen, R. S., & Schmidt, W. 2008, *ApJL*, **688**, L79
- Froebrich, D., & Rowles, J. 2010, *MNRAS*, **406**, 1350
- Ginsburg, A., Bally, J., & Williams, J. P. 2011, *MNRAS*, **418**, 2121
- Ginsburg, A., Robitaille, T., Beaumont, C., & Zuhone, J. 2014, Release Candidate 2—includes yt interop v0.2-rc2, Zenodo, doi:10.5281/zenodo.11485
- Girichidis, P., Konstantin, L., Whitworth, A. P., & Klessen, R. S. 2014, *ApJ*, **781**, 91
- Glover, S. C. O., Federrath, C., Mac Low, M. M., & Klessen, R. S. 2010, *MNRAS*, **404**, 2
- Goodman, A. A., Pineda, J. E., & Schnee, S. L. 2009, *ApJ*, **692**, 91
- Hunter, J. D. 2007, *CSE*, **9**, 90
- Jaupart, E., & Chabrier, G. 2020, *ApJL*, **903**, L2
- Joye, W. A., & Mandel, E. 2003, in ASP Conf. Ser. 295, Astronomical Data Analysis Software and Systems XII, ed. H. E. Payne, R. I. Jedrzejewski, & R. N. Hook (San Francisco, CA: ASP), 489
- Kainulainen, J., Beuther, H., Henning, T., & Plume, R. 2009, *A&A*, **508**, L35
- Kainulainen, J., Federrath, C., & Henning, T. 2014, *Sci*, **344**, 183
- Khullar, S., Federrath, C., Krumholz, M. R., & Matzner, C. D. 2021, *MNRAS*, **507**, 4335
- Kong, S., Lada, C. J., Lada, E. A., et al. 2015, *ApJ*, **805**, 58
- Kritsuk, A. G., Norman, M. L., & Wagner, R. 2011, *ApJL*, **727**, L20
- Kryukova, E., Megeath, S. T., Hora, J. L., et al. 2014, *AJ*, **148**, 11
- Lemaster, M. N., & Stone, J. M. 2008, *ApJL*, **682**, L97
- Lewis, J. A., Lada, C. J., Bieging, J., et al. 2021, *ApJ*, **908**, 76
- Mangum, J. G., & Shirley, Y. L. 2015, *PASP*, **127**, 266
- Murase, T., Handa, T., Matsusaka, R., et al. 2023, *MNRAS*, **523**, 1373
- Murray, N., & Chang, P. 2015, *ApJ*, **804**, 44
- Oliphant, T. E. 2007, *CSE*, **9**, 10
- Padoan, P., & Nordlund, Å 2011, *ApJ*, **730**, 40

- Padoan, P., Nordlund, A., & Jones, B. J. T. 1997, *MNRAS*, 288, 145
- Passot, T., & Vázquez-Semadeni, E. 1998, *PhRvE*, 58, 4501
- Pokhrel, R., Gutermuth, R., Ali, B., et al. 2016, *MNRAS*, 461, 22
- Reipurth, B., & Schneider, N. 2008, in *Handbook of Star Forming Regions, Volume I: The Northern Sky*, ed. B. Reipurth (San Francisco, CA: ASP), 36
- Rosolowsky, E. W., Pineda, J. E., Kauffmann, J., & Goodman, A. A. 2008, *ApJ*, 679, 1338
- Russeil, D., Schneider, N., Anderson, L. D., et al. 2013, *A&A*, 554, A42
- Rygl, K. L. J., Brunthaler, A., Sanna, A., et al. 2012, *A&A*, 539, A79
- Schneider, N., André, P., Könyves, V., et al. 2013, *ApJL*, 766, L17
- Schneider, N., Bontemps, S., Girichidis, P., et al. 2015, *MNRAS*, 453, L41
- Schneider, N., Bontemps, S., Motte, F., et al. 2016, *A&A*, 587, A74
- Schneider, N., Bontemps, S., Simon, R., et al. 2006, *A&A*, 458, 855
- Schneider, N., Ossenkopf-Okada, V., Clarke, S., et al. 2022, *A&A*, 666, A165
- Seligman, D., & Laughlin, G. 2020, *ApJL*, 896, L8
- Shu, F. H. 1977, *ApJ*, 214, 488
- Stutz, A. M., & Kainulainen, J. 2015, *A&A*, 577, L6
- Takekoshi, T., Fujita, S., Nishimura, A., et al. 2019, *ApJ*, 883, 156
- Tremblin, P., Schneider, N., Minier, V., et al. 2014, *A&A*, 564, A106
- van der Tak, F. F. S., Black, J. H., Schöier, F. L., Jansen, D. J., & van Dishoeck, E. F. 2007, *A&A*, 468, 627
- van der Walt, S., Colbert, S. C., & Varoquaux, G. 2011, *CSE*, 13, 22
- Vazquez-Semadeni, E. 1994, *ApJ*, 423, 681
- Virtanen, P., Gommers, R., Oliphant, T. E., et al. 2020, *NatMe*, 17, 261
- Wakelam, V., Bron, E., Cazaux, S., et al. 2017, *MolAs*, 9, 1
- Wang, Y., Beuther, H., Schneider, N., et al. 2020, *A&A*, 641, A53
- Ward, R. L., Wadsley, J., & Sills, A. 2014, *MNRAS*, 445, 1575
- Wilson, T. L. 1999, *RPPh*, 62, 143
- Wright, N. J., Drew, J. E., & Mohr-Smith, M. 2015, *MNRAS*, 449, 741
- Yamagishi, M., Nishimura, A., Fujita, S., et al. 2018, *ApJS*, 235, 9